

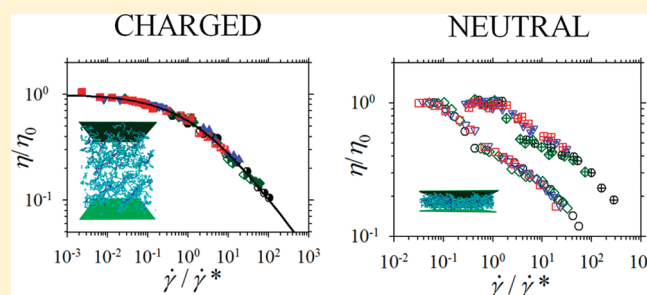
Friction between Brush Layers of Charged and Neutral Bottle-Brush Macromolecules. Molecular Dynamics Simulations

Jan-Michael Y. Carrillo,[†] Daniel Russano,[‡] and Andrey V. Dobrynin^{*,†}

[†]Polymer Program, Institute of Materials Science and Department of Physics, University of Connecticut, Storrs, Connecticut 06269, United States

[‡]Physics Department, Boston University, Boston, Massachusetts 02215, United States

ABSTRACT: Using molecular dynamics simulations, we study the lubricating properties of neutral and charged bottle-brush coatings as a function of the compression and shear stresses and brush grafting density. Our simulations have shown that in charged bottle-brush systems under shear there is a layer with excess counterions located in the middle between brush-bearing surfaces. The main deformation mode of the charged bottle-brush layers is associated with the backbone deformation, resulting in the backbone deformation ratio, α , and shear viscosity, η , being universal functions of the Weissenberg number. In the case of neutral bottle-brush systems, in addition to the backbone deformation there is also side chain deformation. The coupling between backbone and side chain deformation violates universality in the deformation ratio, α , dependence on the Weissenberg number and results in scaling exponents varying with the compression stress and brush grafting density. The existence of different length scales controlling deformation of neutral bottle brushes manifests itself in the shear viscosity, η , dependence on the shear rate, $\dot{\gamma}$. Shear viscosity, η , as a function of the shear rate, $\dot{\gamma}$, has two plateaus and two shear thinning regimes. The low shear rate plateau and shear thinning regime correspond to the backbone deformation, while the second plateau and shear thinning regime at moderate shear rates are due to side chain deformation. For both systems the value of the friction coefficient increases with increasing shear rate. The values of the friction coefficient for charged bottle-brush systems are about ten times smaller than corresponding values for neutral systems at the same shear rate.



1. INTRODUCTION

Brush coatings, layers of polymer chains grafted to the substrate by one end, were shown to significantly reduce sliding friction between surfaces.^{1–7} Experimental studies of friction between sliding surfaces covered with neutral or charged brush layers demonstrated that the values of the friction coefficient can be lower than 10^{-2} in a wide interval of loading forces.^{8–23} In the case of the charged brush layers, the values of the friction coefficient between these coatings are in the range of 0.001–0.03 and are approaching friction coefficients measured for biological surfaces such as articular cartilage coatings.^{24–28} One of the possible explanations of the low values of the friction coefficient between charged brush layers is the osmotic pressure of counterions that precludes strong interpenetration between charged brush layers in comparison with that between neutral brush coatings.

A large number of theoretical^{29–33} and computational^{33–46} studies during the past 20 years were devoted to interaction between brush layers in an attempt to uncover mechanisms responsible for low friction between brush coatings. It was shown that under shear chains in a brush layer begin to deform when the magnitude of the shear rate, $\dot{\gamma}$ (defined as a ratio of the substrate sliding velocity, v_s , to the distance between brush-bearing surfaces, D), exceeds a crossover value, $\dot{\gamma}^*$.³³ Location of the crossover depends on the chain degree of polymerization, solvent quality for the polymer backbone, and

brush grafting density. For neutral brush layers the chain deformation, brush shear viscosity, η , and kinetic friction coefficient, μ , were shown to be universal functions of the Weissenberg number, $W = \dot{\gamma}/\dot{\gamma}^*$.³³ Above the crossover threshold, $W > 1$, in neutral brush systems the chain size along the shear direction increases with increasing Weissenberg number as $R_y \propto W^\beta$ and shear-dependent viscosity decreases as $\eta \propto W^{-\zeta}$. Thus, chain elongation is accompanied by a decrease in overlap between brush layers manifested in shear thinning behavior of a shear viscosity. The particular values of the exponents β and ζ depend on the solvent quality for the polymer backbone and whether the solvent effects were taken into account. Explicit solvent simulations³³ have been able to account for screening of the hydrodynamic interactions between interpenetrating brush layers. These simulations have established scaling relations for chain size, $R_y \propto W^{0.25}$, shear viscosity, $\eta \propto W^{-0.43}$, and kinetic friction coefficient between brush layers, $\mu \propto W^{-0.57}$. This is in agreement with experimental results on polystyrene brushes on mica surfaces.³⁹

Until recently, the majority of the simulation and theoretical studies were devoted to brush layers composed of linear chains.

Received: September 8, 2011

Revised: October 25, 2011

Published: November 10, 2011

There are only a few publications dealing with properties of the brush layers made of bottle-brush macromolecules.^{47–51} The properties of neutral bottle-brush layers were studied in the framework of the scaling⁴⁷ and self-consistent field⁵¹ approaches. Computer simulations have addressed the structure of the charged and neutral bottle-brush layers^{48,49} and interaction between brush layers upon compression.⁵⁰ It was confirmed that charged bottle-brush layers begin to interact long before they come into physical contact.⁵⁰ In this regime the interaction between two brush layers is due to diffusive counterion clouds that are formed outside the edges of the brush layers. At these separations brush layers can be considered as charged surfaces with effective surface charge densities whose magnitudes depend on the fraction of the condensed within brush counterions.⁵⁰ It is important to point out that the counterion condensation within bottle-brush layers is a multiscale process which reflects the structure of the bottle-brush macromolecules.⁴⁸ In the interval of the brush separations, when two brush layers overlap, the disjoining pressure, P , scales with substrate separation, D , and brush grafting density, ρ_g , as $P \propto \rho_g^{1.5 \pm 0.2} D^{-1.8 \pm 0.2}$ for charged and $P \propto \rho_g^{2.4 \pm 0.2} D^{-4.6 \pm 0.3}$ for neutral bottle-brush layers.⁵⁰ These scaling laws of the disjoining pressure dependence on the distance D between brush-bearing surfaces are qualitatively different from those observed for systems of charged and neutral brushes made of flexible linear chains. This difference was explained by the dominant contribution of the bending energy of the bottle-brush macromolecules to the interaction potential between brush layers.

In this paper we present results of the molecular dynamics simulations of the sliding friction between layers made of neutral and charged bottle-brush macromolecules as a function of the brush grafting density, load pressure, and shearing force. The simulations were performed without explicit solvent. This corresponds to the Rouse dynamics⁵² of the brush layers. Comparison between charged and neutral brush systems allowed us to elucidate the role of the electrostatic interactions and osmotic pressure of counterions on the brush lubricating properties. The rest of the paper is organized as follows: In section 2 we describe our model of bottle-brush macromolecules and the simulation procedure. In section 3 we illustrate how electrostatic interactions influence bottle-brush deformation under shear and brush layer interpenetration and its effect on the friction coefficient between brush layers. Finally, in section 4 we discuss our result.

2. SIMULATION DETAILS

We performed molecular dynamics simulations⁵³ of interactions between grafted layers of charged and neutral bottle-brush macromolecules. For charged bottle-brush systems counterions were included explicitly. The bottle-brush macromolecules were modeled by chains of Lennard-Jones (LJ) particles (beads) with diameter σ . Each bottle-brush macromolecule consisted of a main chain with degree of polymerization $N = 97$ and side chains with degree of polymerization $m = 21$ (see Figure 1). (The bottle-brush model is similar to the one used in our simulations of bottle-brush layers.^{48,50}) There were 31 side chains per bottle-brush macromolecule, which corresponds to every third monomer of the main chain having a side chain attached to it. For charged bottle-brush macromolecules, only side chains were charged, with the fraction of the charged monomers $f = 1/3$ corresponding to every third monomer carrying a negative electrical charge, $-e$. N_B bottle-brush macromolecules were grafted to a substrate. There were two substrates per simulation box located at the beginning of the simulation run at $z = 0$ and $z = L_z$. Each substrate was modeled by a periodic hexagonally packed lattice of beads composed of 80×70 beads with diameter σ . The brush

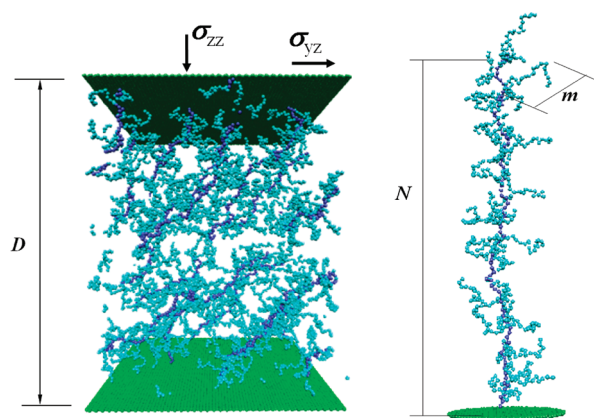


Figure 1. Snapshot of the simulation box with charged bottle brushes (left) and the bottle-brush macromolecule (right).

grafting density of the substrate, ρ_g , was equal to $1.24 \times 10^{-3} \sigma^{-2}$, $2.06 \times 10^{-3} \sigma^{-2}$, $3.09 \times 10^{-3} \sigma^{-2}$, and $4.33 \times 10^{-3} \sigma^{-2}$. The system dimensions in the xy -plane were $70.0 \sigma \times 69.28 \sigma$. The initial height of the simulation box, L_z , was set to 200.0σ for all simulations. The top substrate with the bottle-brush layer was allowed to move along the z -direction and y -direction to model brush compression and shear.

All particles in the system interacted through truncated-shifted LJ potential:

$$U_{LJ}(r_{ij}) = \begin{cases} 4\epsilon_{LJ} \left[\left(\frac{\sigma}{r_{ij}} \right)^{12} - \left(\frac{\sigma}{r_{ij}} \right)^6 - \left(\frac{\sigma}{r_{cut}} \right)^{12} + \left(\frac{\sigma}{r_{cut}} \right)^6 \right] & r \leq r_{cut} \\ 0 & r > r_{cut} \end{cases} \quad (1)$$

where r_{ij} is the distance between the i th and j th beads and σ is the bead diameter, chosen to be the same regardless of the bead type. The cut-off distance $r_{cut} = 2.5 \sigma$ was set for polymer–polymer interactions, and $r_{cut} = 2^{1/6} \sigma$ was selected for all other pairwise interactions. The interaction parameter, ϵ_{LJ} , was equal to $k_B T$ for polymer–counterion, counterion–counterion, polymer–substrate, and counterion–substrate interactions, where k_B is the Boltzmann constant and T is the absolute temperature. The value of the Lennard-Jones interaction parameter for the polymer–polymer pairs was set to $0.3 k_B T$, which is close to a Θ solvent condition for the polymer.⁵⁴ By selecting the strength of the polymer–polymer interactions close to the Θ -point, we minimized the effect of the short-range interactions on the bottle-brush properties.

The connectivity of monomers into bottle-brush macromolecules was maintained by the finite extension nonlinear elastic (FENE) potential:⁵⁵

$$U_{FENE}(r) = -\frac{1}{2} k_{spring} R_{max}^2 \ln \left(1 - \frac{r^2}{R_{max}^2} \right) \quad (2)$$

with the spring constant $k_{spring} = 30 k_B T / \sigma^2$ and maximum bond length $R_{max} = 1.5 \sigma$. The repulsive part of the bond potential was represented by the truncated-shifted LJ potential with $\epsilon_{LJ} = k_B T$ and $r_{cut} = 2^{1/6} \sigma$.

In the case of charged bottle-brush layers, electrostatic interaction between any two charged particles (charged monomers and counterions) with charge valences q_i and q_j , and separated by a distance r_{ij} , was given by the Coulomb potential:

$$U_{Coul}(r_{ij}) = k_B T \frac{l_B q_i q_j}{r_{ij}} \quad (3)$$

where $l_B = e^2 / \epsilon k_B T$ is the Bjerrum length, defined as the length scale at which the Coulomb interaction between two elementary charges e , in a dielectric medium with dielectric constant ϵ , is equal to the thermal

energy, $k_B T$. In our simulations, the value of the Bjerrum length, l_B , was equal to 1.0σ .

The particle–particle particle-mesh (PPPM) method⁵⁶ implemented in LAMMPS⁵⁷ with the sixth-order charge interpolation scheme and estimated accuracy of 10^{-5} was used for calculations of the electrostatic interactions between all charges in the system. The 2D periodic images of the system were periodically replicated along the z -direction with distance $L = 3L_z$ between their boundaries. This reduced the problem of calculation of the electrostatic interactions in a 2D periodic system to those in a 3D system.⁵⁸

In our simulations, the top substrate was subjected to a constant shear stress, σ_{yz} , and normal compression stress, σ_{zz} (see Figure 1). This was achieved by applying constant shear and compression forces, f_y and f_z , to each bead forming the top substrate. The magnitudes of the shear and compression stresses are related to the magnitudes of the shear and compression forces, f_y and f_z , as follows: $\sigma_{yz} = f_y/a_0$ and $\sigma_{zz} = f_z/a_0$, where $a_0 = 0.866 \sigma^2$ is the surface area per substrate bead. These simulations were performed to obtain the relationship between the substrate velocity and magnitudes of the normal and shear stresses. To maintain a constant temperature during these simulations, we applied a Langevin thermostat along the vorticity direction (x -axis) only.⁵⁹ The equation of motion of the i th bead in this case was

$$m \frac{d\vec{v}_i(t)}{dt} = \vec{F}_i(t) - \xi \vec{v}_i(t) + \vec{F}_i^R(t) \quad (4)$$

where the stochastic force \vec{F}_i^R had only an x -component with zero average value, $\langle \vec{F}_i^R(t) \rangle = 0$, and δ -functional correlations, $\langle \vec{F}_i^R(t) \cdot \vec{F}_i^R(t') \rangle = 2\xi k_B T \delta(t - t')$. The mass, m , was set to unity for all particles. The friction coefficient, ξ , was equal to $0.143m/\tau_{LJ}$, where τ_{LJ} is the standard LJ time, $\tau_{LJ} = \sigma(m/\epsilon_{LJ})^{1/2}$. The velocity-Verlet algorithm with time step $\Delta t = 0.01 \tau_{LJ}$ was used for integration of the equations of motion (eq 4) for all our systems except the charged bottle-brush system with a brush grafting density of $4.33 \times 10^{-3} \sigma^{-2}$, shear force $f_y = 0.004 k_B T/\sigma$, and compression force $f_z = 0.003 k_B T/\sigma$, for which the integration step was set to $\Delta t = 0.005 \tau_{LJ}$. This was done to achieve a better temperature control in a weakly interacting brush system. All simulations were performed using LAMMPS.⁵⁷

Simulations were done using the following procedure: At the beginning of each simulation run, the main and side chains of the bottle-brush macromolecules were in a fully extended conformation with the main chains pointing parallel to the z -axis and side chains randomly oriented in the x - y plane. In the case of the charged systems, neutralizing monovalent counterions were uniformly distributed over the volume of the simulation box. Systems were pre-equilibrated for up to $4 \times 10^4 \tau_{LJ}$. This was followed by the simulation runs lasting up to $7 \times 10^4 \tau_{LJ}$. The last $2 \times 10^4 \tau_{LJ}$ was used for data analysis. The actual durations of the simulation runs for each system were determined by monitoring the time evolution of the chain size and displacement of the center of mass of the top substrate to ensure that both quantities have reached a steady-state regime.

3. SIMULATION RESULTS

Parts a and b of Figure 2 show the dependence of the top substrate velocity on the magnitude of the shear stress for two different values of the compression stress applied to the top substrate, $\sigma_{zz} = 3.46 \times 10^{-3} k_B T/\sigma^3$ and $\sigma_{zz} = 3.46 \times 10^{-2} k_B T/\sigma^3$. For both values of the compression stresses, the charged systems demonstrate larger values of velocity of the top substrate for all brush grafting densities in comparison with that for neutral systems. In the case of low compression (see Figure 2a), the substrate velocity of charged bottle-brush systems is almost independent of the brush grafting densities. Only a system with the lowest brush grafting density, $\rho_g = 1.24 \times 10^{-3} \sigma^{-2}$, has

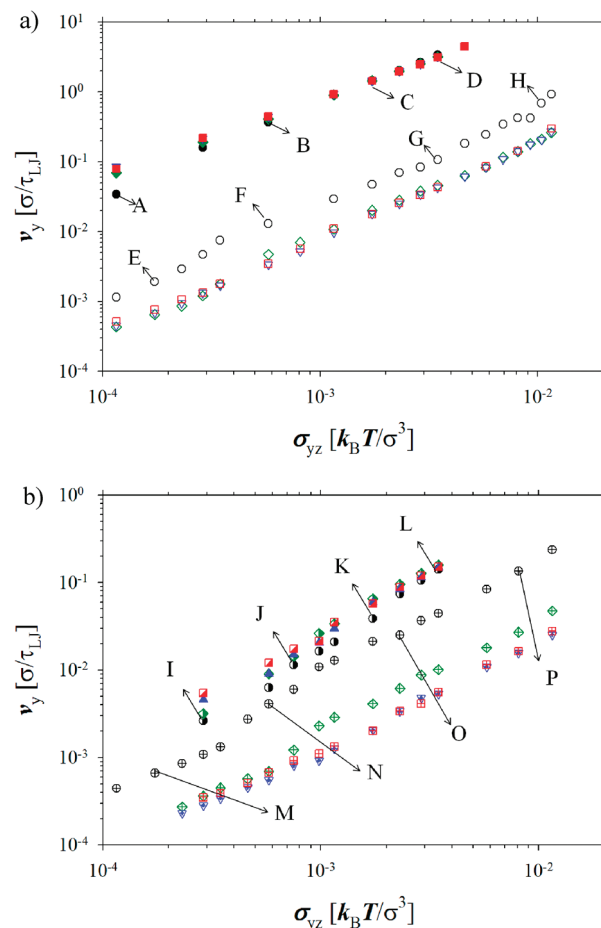


Figure 2. Dependence of the shear velocity, v_y , on shear stress, σ_{yz} , at low compression stress, $\sigma_{zz} = 3.46 \times 10^{-3} k_B T/\sigma^3$ (a), and high compression stress, $\sigma_{zz} = 3.46 \times 10^{-2} k_B T/\sigma^3$ (b), for bottle-brush layers at different grafting densities: $\rho_g = 1.24 \times 10^{-3} \sigma^{-2}$ (charged low compression, \bullet ; neutral low compression, \circ); charged high compression, \ominus ; neutral high compression, \oplus), $\rho_g = 2.06 \times 10^{-3} \sigma^{-2}$ (charged low compression, \blacklozenge ; charged high compression, half-shaded tilted square; neutral low compression, \diamond ; neutral high compression, plus sign inside tilted square), $\rho_g = 3.09 \times 10^{-3} \sigma^{-2}$ (charged low compression, \blacktriangledown ; neutral low compression, ∇ ; charged high compression, \blacktriangle ; neutral high compression, plus sign inside inverted triangle), and $\rho_g = 4.33 \times 10^{-3} \sigma^{-2}$ (charged low compression, \blacksquare ; neutral low compression, \square ; charged high compression, \blacksquare ; neutral high compression, \boxplus). Letters A–P correspond to snapshots of bottle-brush macromolecules and the layer structure at different shear and compression loads shown in Figure 3.

a lower velocity of the top substrate in the range of shear stresses σ_{yz} smaller than $10^{-3} k_B T/\sigma^3$. At the same magnitude of the compression stress, substrates covered with brush layers having the lowest brush grafting densities are separated by smaller distances and demonstrate larger overlap between brush coatings in comparison with brushes having higher brush grafting densities. This results in higher effective friction between substrates and leads to lower substrate velocity. With increasing magnitude of the shear stress, the bottle-brush chains tilt and stretch (see images A–D in Figure 3). For charged bottle-brush systems, there is always a layer of “lubricating” counterions separating two brush layers. This is illustrated in Figure 4 showing the distribution of the excess charge throughout the gap between substrates. It follows

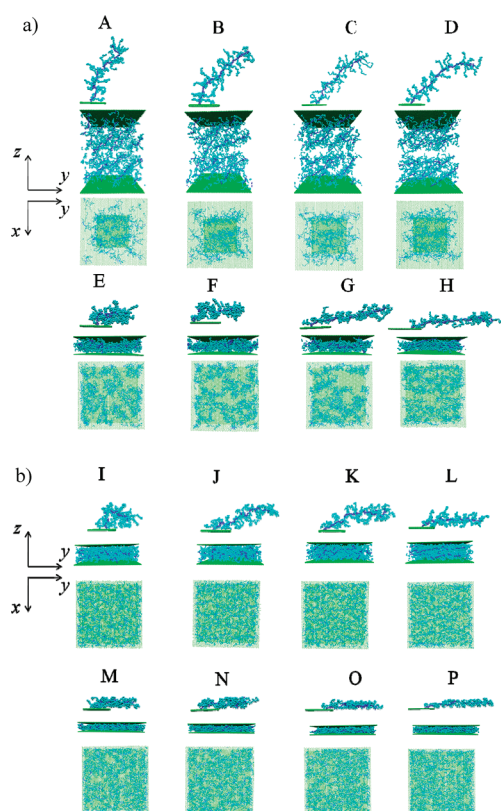


Figure 3. Snapshots of the bottle-brush layers at different shear velocities for low compression load, $\sigma_{zz} = 3.46 \times 10^{-3} k_B T / \sigma^3$ (a), and high compression load, $\sigma_{zz} = 3.46 \times 10^{-2} k_B T / \sigma^3$ (b).

from this figure that inside bottle-brush layer counterions compensate bottle-brush charge. There are regions of the charge imbalance close to the grafting substrates and to the edges of the brush layers. The lubricating layer of counterions is responsible for the large values of the sliding velocities observed in charged brush systems (see Figure 2a).

The situation is different in the case of the neutral bottle-brushes. In this case, the brush layers with the lowest bottle-brush grafting density, $\rho_g = 1.24 \times 10^{-3} \sigma^{-2}$, slide with the largest velocities while the brush layers with $\rho_g > 1.24 \times 10^{-3} \sigma^{-2}$ have close values of the substrate velocity in the entire interval of the shear stresses. This is due to the fact that at high brush grafting densities the bottle-brushes mostly interact through the side chains. It is worth pointing out that a neutral bottle-brush macromolecule experiences larger relative elongation in the direction of shear than charged bottle-brushes (see images A–H in Figure 3a). Both charged and neutral bottle-brush macromolecules demonstrate stronger orientational alignment along the y -axis with increasing shear stress.

In the higher compression case (see Figure 2b), all systems demonstrate lower values of the sliding velocity in comparison with the low compression case. In addition, we observed a stronger dependence of the sliding velocities on the brush grafting densities. This is due to stronger overlap between bottle-brush layers as seen in Figure 3b. Note that for this compression stress neutral bottle-brush macromolecules are already oriented along the shear direction (y -axis) even at low values of the shear stresses. For charged bottle-brush systems we still see convergence of the velocity curves at shear stresses

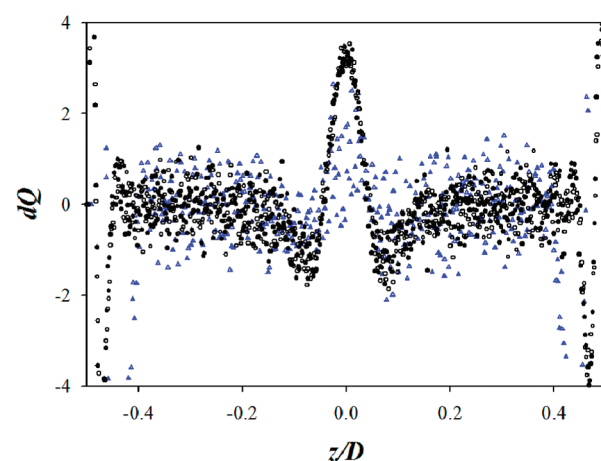


Figure 4. Charge distributions in bottle-brush layers at different values of the compression stress, $\sigma_{zz} = 3.46 \times 10^{-3} k_B T / \sigma^3$ (black circles) and $\sigma_{zz} = 3.46 \times 10^{-2} k_B T / \sigma^3$ (blue triangles), and shear stress, $\sigma_{yz} = 0.0 k_B T / \sigma^3$ (filled symbols) and $\sigma_{yz} = 3.46 \times 10^{-3} k_B T / \sigma^3$ (open symbols).

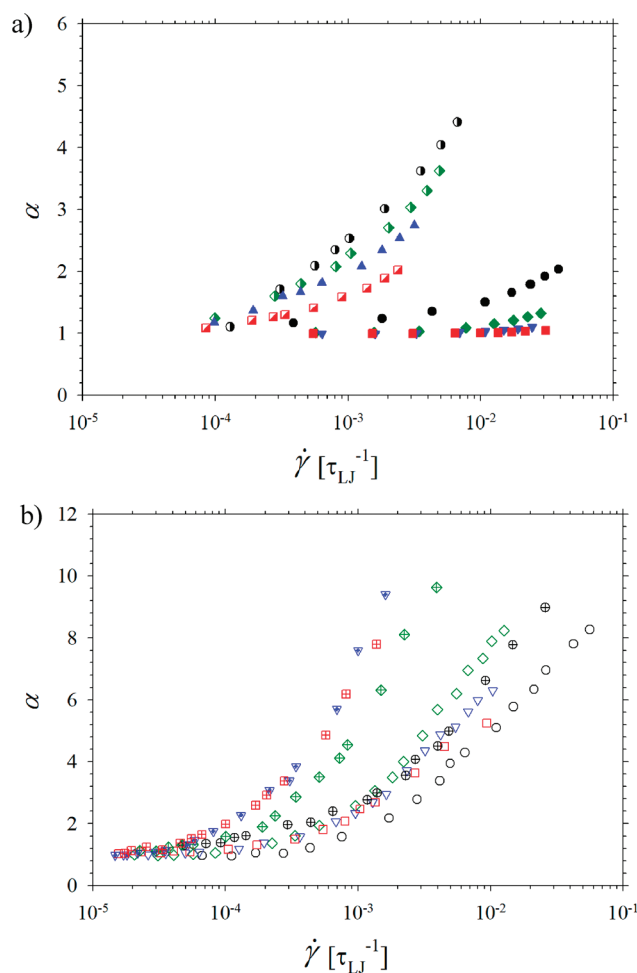


Figure 5. Dependence of the deformation ratio, α , on the shear rate, $\dot{\gamma}$, for charged (a) and neutral (b) bottle-brush layers at different compression loads and grafting densities. Notations are the same as in Figure 2.

larger than $2 \times 10^{-3} k_B T / \sigma^3$. As in the case of low compression stress, this can be explained by the appearance of a lubricating

Table 1. Dependence of the Crossover Shear Rate and Exponent β on the Brush Grafting Density

$\rho_g (\sigma^{-2})$	$\dot{\gamma}^* (\tau_{LJ}^{-1})$			
	charged		neutral	
	low compression ^a	high compression ^b	low compression	high compression
1.24×10^{-3}	$(4.3 \pm 0.8) \times 10^{-3}$	$(6.3 \pm 0.8) \times 10^{-5}$	$(1.0 \pm 0.1) \times 10^{-3}$	$(9.3 \pm 0.9) \times 10^{-5}$
2.06×10^{-3}	$(2.1 \pm 0.2) \times 10^{-2}$	$(8.2 \pm 0.4) \times 10^{-5}$	$(3.9 \pm 0.5) \times 10^{-4}$	$(5.2 \pm 0.6) \times 10^{-5}$
3.09×10^{-3}	$(7.8 \pm 1.0) \times 10^{-2}$	$(1.3 \pm 0.1) \times 10^{-4}$	$(4.5 \pm 0.3) \times 10^{-4}$	$(5.2 \pm 0.7) \times 10^{-5}$
4.33×10^{-3}	$(2.3 \pm 0.6) \times 10^{-1}$	$(2.9 \pm 0.2) \times 10^{-4}$	$(4.9 \pm 0.3) \times 10^{-4}$	$(5.2 \pm 0.4) \times 10^{-5}$

$\rho_g (\sigma^{-2})$	β			
	charged		neutral	
	low compression ^a	high compression ^b	low compression	high compression
1.24×10^{-3}	0.32 ± 0.01	0.32 ± 0.01	0.77 ± 0.05	0.41 ± 0.01
2.06×10^{-3}	0.32 ± 0.01	0.32 ± 0.01	0.77 ± 0.05	0.53 ± 0.02
3.09×10^{-3}	0.32 ± 0.01	0.32 ± 0.01	0.77 ± 0.05	0.65 ± 0.03
4.33×10^{-3}	0.32 ± 0.01	0.32 ± 0.01	0.77 ± 0.05	0.65 ± 0.03

^a $\sigma_{zz} = 3.46 \times 10^{-3} k_B T / \sigma^3$. ^b $\sigma_{zz} = 3.46 \times 10^{-2} k_B T / \sigma^3$.

layer of counterions separating two bottle-brush layers (see Figure 4).

To quantify bottle-brush deformation under shear, in parts a and b of Figure 5 we show the dependence of the deformation ratio of the bottle-brush backbone:

$$\alpha = \frac{\langle R_e^2(\dot{\gamma}) \rangle}{\langle R_e^2(0) \rangle} \quad (5)$$

where $\langle R_e^2(\dot{\gamma}) \rangle$ is the mean square value of the backbone end-to-end distance at the shear rate

$$\dot{\gamma} = \frac{v_y}{D} \quad (6)$$

and $\langle R_e^2(0) \rangle$ is its value at zero shear rate. The values of $\langle R_e^2(0) \rangle$ were obtained from simulations with zero shear stress. (Note that eq 6 is just a definition of the shear rate and the actual velocity profiles could be nonlinear across the gap with thickness D .) The characteristic feature of all curves is that the bottle-brush backbone starts to deform when the value of the shear rate exceeds the crossover value of the shear rate, $\dot{\gamma}^*$. It follows from these plots that charged bottle-brush systems have smaller values of the deformation ratio, α , than the neutral bottle-brushes at the same value of the shear rate (stress). This can be explained by the larger initial elongation of charged bottle-brushes caused by electrostatic interactions.⁵⁰ Thus, to overcome electrostatically induced tension of the bottle-brush backbone, one has to apply larger shear stress.

To determine the crossover value of the shear rate, $\dot{\gamma}^*$, we have fitted the bottle-brush deformation curves shown in Figure 5 to the following equation:

$$\alpha = \frac{\langle R_e^2(\dot{\gamma}) \rangle}{\langle R_e^2(0) \rangle} = \left(1 + \frac{\dot{\gamma}}{\dot{\gamma}^*} \right)^\beta \quad (7)$$

considering $\dot{\gamma}^*$ and β as fitting parameters. This is one possible form of the scaling function describing bottle-brush deformation under shear. The values of the fitting parameters are summarized

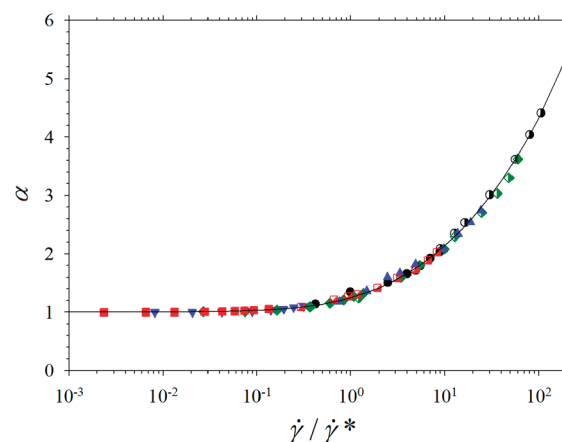


Figure 6. Dependence of the deformation ratio, α , on the Weissenberg number, $W = \dot{\gamma} / \dot{\gamma}^*$, for charged bottle-brush layers at different compression loads and grafting densities: $\rho_g = 1.24 \times 10^{-3} \sigma^{-2}$ (low compression, \bullet ; high compression, \circ), $\rho_g = 2.06 \times 10^{-3} \sigma^{-2}$ (low compression, \blacklozenge ; high compression, half-shaded tilted square), $\rho_g = 3.09 \times 10^{-3} \sigma^{-2}$ (low compression, \blacktriangledown ; high compression, \blacktriangle), and $\rho_g = 4.33 \times 10^{-3} \sigma^{-2}$ (low compression, \blacksquare ; high compression, \blacksquare). The line corresponds to the best fit to eq 7 with $\beta = 0.32$. The values of $\dot{\gamma}^*$ are given in Table 1.

in Table 1. For charged bottle-brushes all data sets can be fitted simultaneously by considering $\dot{\gamma}^*$ for each set and β as independent fitting parameters. From this fitting procedure the value of the exponent β was equal to 0.32. The value of the crossover shear rate, $\dot{\gamma}^*$, monotonically increases with increasing brush grafting density for both values of the compression stress. Also the value of $\dot{\gamma}^*$ decreases by about 2–3 orders of magnitude by increasing the compression stress by one order of magnitude. This reflects an increase of the interaction between two brush layers with increasing brush compression. In Figure 6 we replotted bottle-brush deformation data as a function of the Weissenberg number, $W = \dot{\gamma} / \dot{\gamma}^*$. All data sets have collapsed into one master curve. This confirms the existence of a single characteristic time

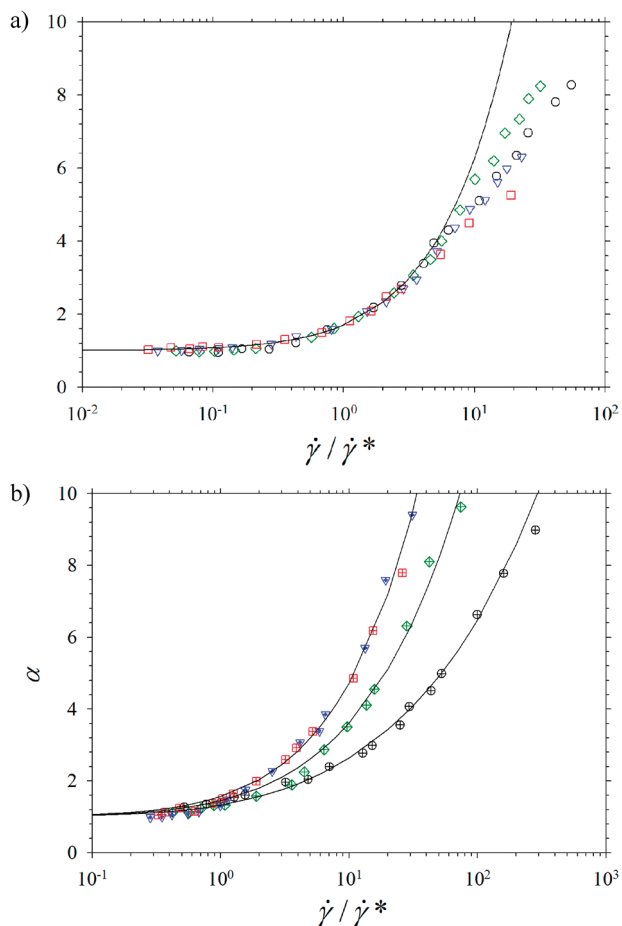


Figure 7. Dependence of the deformation ratio, α , on the Weissenberg number, $W = \dot{\gamma}/\dot{\gamma}^*$, for neutral bottle-brush layers at low compression load, $\sigma_{zz} = 3.46 \times 10^{-3} k_B T/\sigma^3$ (a), and high compression load, $\sigma_{zz} = 3.46 \times 10^{-2} k_B T/\sigma^3$ (b), and different brush grafting densities: $\rho_g = 1.24 \times 10^{-3} \sigma^{-2}$ (low compression, \circ ; high compression, \oplus), $\rho_g = 2.06 \times 10^{-3} \sigma^{-2}$ (low compression, \diamond ; high compression, plus sign inside tilted square), $\rho_g = 3.09 \times 10^{-3} \sigma^{-2}$ (low compression, ∇ ; high compression, plus sign inside inverted triangle), and $\rho_g = 4.33 \times 10^{-3} \sigma^{-2}$ (low compression, \square ; high compression, \boxplus). The lines correspond to the best fit to eq 7. The values of the fitting parameters are given in Table 1.

and length scale which controls deformation of the charged bottle-brush under shear. Similar universal behavior was observed for brushes of linear chains.³³ This indicates that in this range of compression and shear stresses one can effectively consider a charged bottle-brush macromolecule as a linear chain with effective persistence length. This point of view is also consistent with our previous results on bottle-brush compression.⁵⁰

The situation is qualitatively different in the case of the neutral bottle-brushes. In this case only data corresponding to low compression stress can be fitted together, resulting in the same value of the exponent $\beta = 0.77$ for all data sets. The fitting of the high compression data results in values of the exponent β being dependent on the brush grafting densities. In Figure 7 we replotted bottle-brush deformation data as a function of the Weissenberg number, W . While high compression data show a good agreement with eq 7 throughout the entire interval of the Weissenberg numbers, the low compression data begin to deviate when W exceeds 10. It is also interesting to point out that the obtained values of the crossover shear rate, $\dot{\gamma}^*$, change nonmonotonically

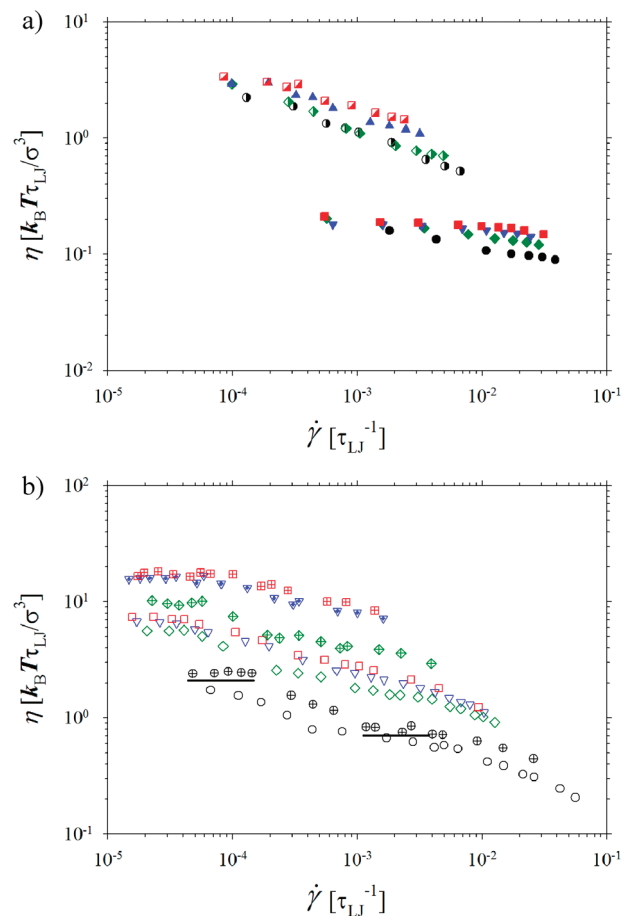


Figure 8. Dependence of the shear viscosity, η , on the shear rate, $\dot{\gamma}$, for charged (a) and neutral (b) bottle-brush layers at different compression stresses and grafting densities: $\rho_g = 1.24 \times 10^{-3} \sigma^{-2}$ (charged low compression, \bullet ; neutral low compression, \circ); charged high compression, \blacklozenge ; neutral high compression, \oplus), $\rho_g = 2.06 \times 10^{-3} \sigma^{-2}$ (charged low compression, \blacklozenge ; charged high compression, half-shaded tilted square; neutral low compression, \diamond ; neutral high compression, plus sign inside tilted square), $\rho_g = 3.09 \times 10^{-3} \sigma^{-2}$ (charged low compression, \blacktriangledown ; neutral low compression, ∇ ; charged high compression, \blacktriangle ; neutral high compression, plus sign inside inverted triangle), and $\rho_g = 4.33 \times 10^{-3} \sigma^{-2}$ (charged low compression, \blacksquare ; neutral low compression, \square ; charged high compression, \blacksquare ; neutral high compression, \boxplus).

with the brush grafting density (see Table 1). Also the values of $\dot{\gamma}^*$ for charged systems are always higher than corresponding values obtained for neutral bottle-brushes. This is in agreement with the observation that charged bottle-brush macromolecules are more stretched; thus, their deformation requires high shear rates.

The energy dissipation in sliding bottle-brush layers is controlled by the shear viscosity:

$$\eta(\dot{\gamma}) = \frac{\sigma_{yz}(\dot{\gamma})}{\dot{\gamma}} \quad (8)$$

Parts a and b of Figure 8 show the dependence of the shear viscosity on the shear rate, $\dot{\gamma}$. The charged systems show shear thinning behavior with increasing magnitude of the shear rate. This is consistent with a decrease in the number of contacts between two brush layers and formation of the lubricating layer of counterions with increasing shear rate. In the case of the neutral bottle-brushes,

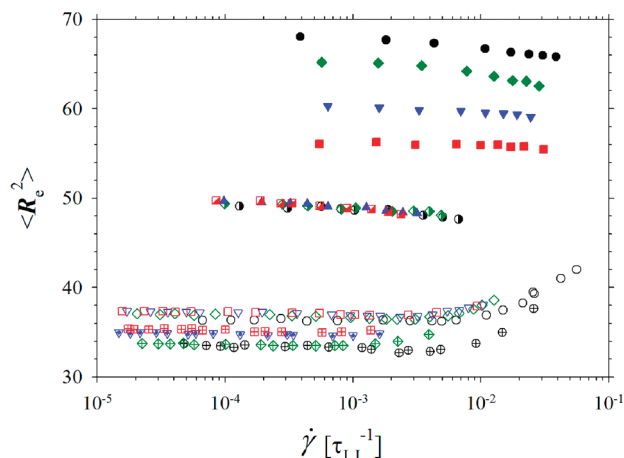


Figure 9. Dependence of the mean square end-to-end distance of the side chains on the shear rate, $\dot{\gamma}$, for charged and neutral bottle-brush layers at different compression stresses and grafting densities. Notations are the same as in Figure 8.

the situation is more complicated. There are two plateau regimes and two shear thinning regimes in shear viscosity, $\eta(\dot{\gamma})$, as a function of the shear rate, $\dot{\gamma}$. The low shear rate plateau corresponds to the linear regime, $\sigma_{yz}(\dot{\gamma}) \propto \dot{\gamma}$. In this interval of the shear rates, shear viscosity saturates and approaches zero shear rate viscosity, η_0 . The second plateau is located at the intermediate interval of the shear rates. This plateau is more pronounced for brush layers with the lowest brush grafting densities. It becomes less pronounced with increasing brush grafting density and magnitude of the compression stress. One can attribute the appearance of the second plateau to deformation of the side chains. Typical bottle-brush configurations shown in parts a (G, H) and b (N–P) of Figure 3 illustrate that at high shear rates (or high sliding velocities) the bottle-brush backbone is strongly oriented along the grafting surface such that the local bottle-brush structure resembles that of a planar brush of linear chains. Thus, the second plateau regime represents a crossover from the bottle-brush backbone deformation regime to the bottle-brush side chain deformation regime. To further support this observation, in Figure 9 we plot the dependence of the mean square value of the end-to-end distance of the side chains as a function of the shear rate. The crossover to the second shear thinning regime correlates with the upturn in the end-to-end distance curves shown in Figure 9. It is also important to point out that for the charged systems the size of the side chains stays almost constant in the entire range of the shear rates. The small decrease in the side chain size occurs at the interval of shear rates where the average distance between grafting substrates experiences a small decrease.

Using data for the crossover values of the shear rates and zero shear rate viscosity evaluated from Figure 8, we can try to collapse all our data for charged bottle-brush systems. Unfortunately, we do not know the zero shear rate viscosity for all our data sets due to the large uncertainty in determining the zero shear rate viscosity for small values of the shear stress and shear rate. To overcome this problem, we have assumed that data sets can be described by the following crossover function throughout the entire interval of the Weissenberg numbers, $W = \dot{\gamma}/\dot{\gamma}^*$:⁶⁰

$$\eta_i(W) = \frac{\eta_0^i}{1 + AW^\zeta} \quad (9)$$

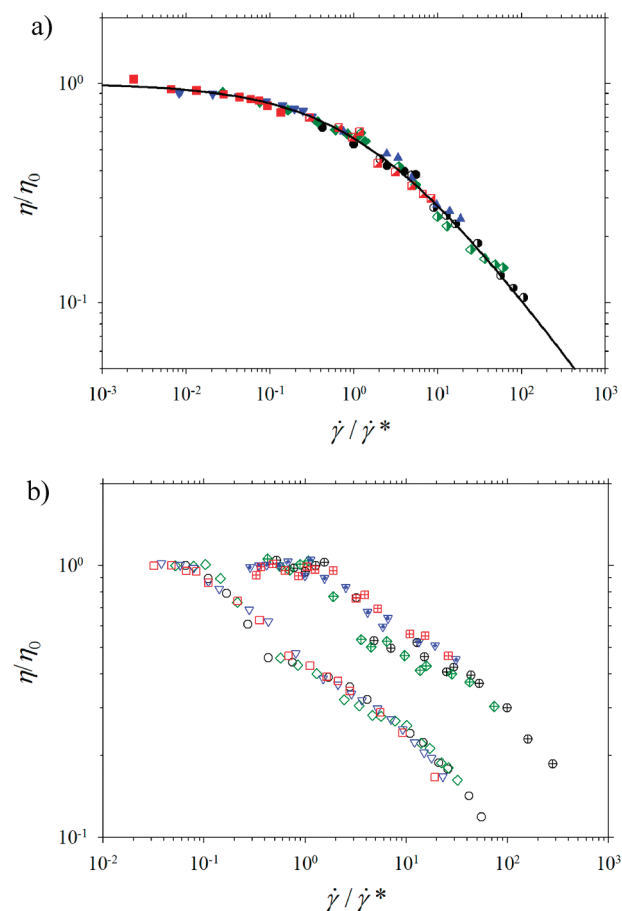


Figure 10. Dependence of the reduced shear viscosity, η/η_0 , on the Weissenberg number, $W = \dot{\gamma}/\dot{\gamma}^*$, for charged (a) and neutral (b) bottle-brush layers at different compression stresses and grafting densities. Notations are the same as in Figure 8. The solid line in (a) is the best fit to eq 9 with $\zeta = 0.53 \pm 0.04$ and $A = 0.78 \pm 0.02$. The values of the zero shear rate viscosity are given in Table 2.

Table 2. Zero Shear Rate Viscosity

$\rho_g (\sigma^{-2})$	$\eta_0 (k_B T \tau_{LJ} / \sigma^3)$			
	charged		neutral	
	low compression ^a	high compression ^b	low compression	high compression
1.24×10^{-3}	0.25 ± 0.02	4.91 ± 0.2	1.7 ± 0.1	2.5 ± 0.1
2.06×10^{-3}	0.22 ± 0.01	4.90 ± 0.4	5.6 ± 0.3	9.8 ± 0.4
3.09×10^{-3}	0.20 ± 0.01	4.89 ± 0.4	6.6 ± 0.1	15.9 ± 0.7
4.33×10^{-3}	0.20 ± 0.01	4.85 ± 0.3	7.4 ± 0.2	18.0 ± 0.6

^a $\sigma_{zz} = 3.46 \times 10^{-3} k_B T / \sigma^3$. ^b $\sigma_{zz} = 3.46 \times 10^{-2} k_B T / \sigma^3$.

We fitted all charged bottle-brush data sets simultaneously by considering A , ζ , and η_0^i as adjustable parameters. The results of this fitting procedure are summarized in Table 2. The universal plot for charged bottle-brushes is shown in Figure 10a. The obtained values of the zero shear rate viscosity decrease with increasing charged bottle-brush grafting density.

For neutral systems we can estimate the value of the zero shear rate viscosity from the plateau regime at low shear rates

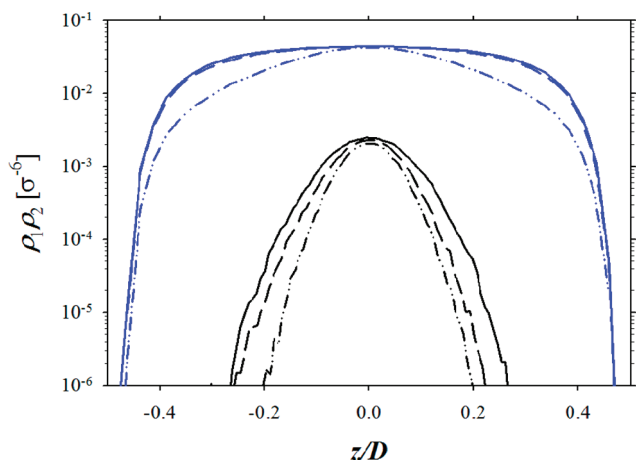


Figure 11. Overlap function $\rho_1(z)\rho_2(z)$ between bottle-brush layers for charged (black lines) and neutral (blue lines) high compression load systems at grafting density $\rho_g = 4.33 \times 10^{-3} \sigma^{-2}$ and different Weissenberg numbers, W , equal to 0.0 (—), 0.9 (---), and 3.1 (- · -).

(see Figure 8b). Using these values of the zero shear rate viscosity (see Table 2) and the crossover value of the shear rates (see Table 1), we can replot data shown in Figure 8b in terms of the reduced viscosity, η/η_0 , and Weissenberg number, $W = \dot{\gamma}/\dot{\gamma}^*$. However, for neutral systems the data collapse is not as good as for charged systems (see Figure 10b). For low compression data the first shear thinning regime begins at $W \approx 0.1$, which is about one order in magnitude below the crossover value of the Weissenberg number for the bottle-brush backbone deformation (see Figure 7a). The second shear thinning regime starts at $W \approx 2$. For higher compression data, the first crossover is located at $W \approx 1$ while the second one is located at $W \approx 20$. The largest spread of the data is observed at the intermediate range of the Weissenberg numbers where the crossover between the backbone deformation regime and side chain deformation regime takes place. It is also evident from this figure that the reduced viscosity data sets for low and high compressions are shifted with respect to each other by a factor. Thus, crossover to the shear thinning regime depends on the magnitude of the compression stress. This should not be surprising since compression controls bottle-brush overlap and the number of binary contacts responsible for energy dissipation within overlapping brush layers. It is also important to point out that the value of the zero shear rate viscosity, η_0 , increases with increasing brush grafting density. This behavior is opposite what we have seen for charged systems (see Table 2).

It is important to point out that the observed shear thinning behavior in shear rate dependent viscosity is a macroscopic manifestation of the decrease in the number of contacts between two brush layers with increasing shear rate. The overlap between two layers is characterized by the product $\rho_1(z)\rho_2(z)$ of the bottle-brush monomer densities from the bottom, $\rho_1(z)$, and top, $\rho_2(z)$, substrates. In the region where two bottle-brush layers overlap, this quantity is nonzero. Figure 11 shows the dependence of the product $\rho_1(z)\rho_2(z)$ for charged and neutral brush layers at different values of the Weissenberg number. The maximum of the overlap function obtained for charged systems is significantly smaller than the magnitude of this function corresponding to neutral bottle-brush systems. The width of the overlap region is narrower for charged systems as well. Note that for both systems

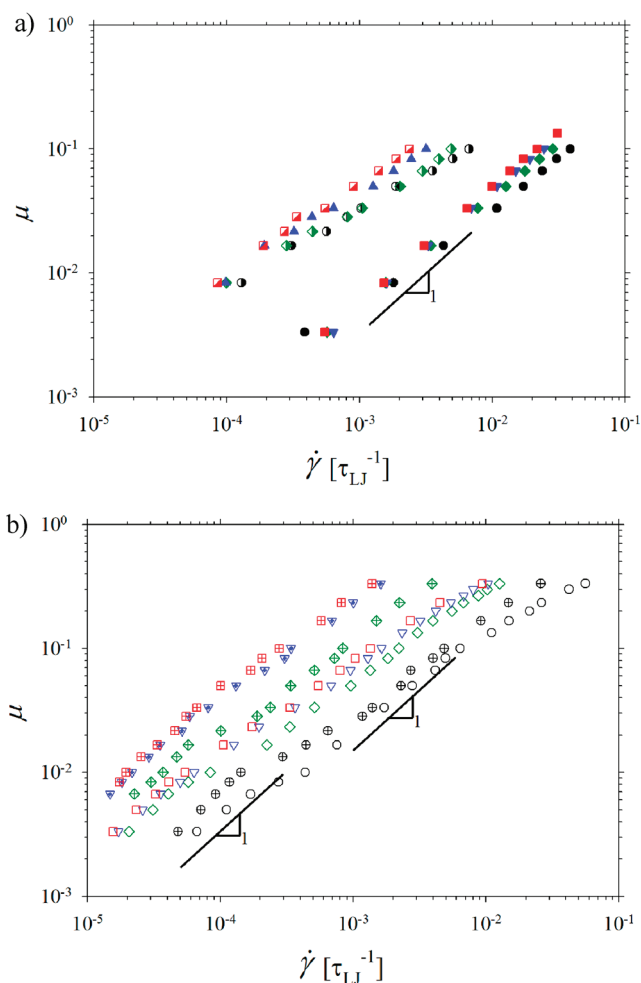


Figure 12. Dependence of the friction coefficient, μ , on the shear rate, $\dot{\gamma}$, for charged (a) and neutral (b) bottle-brush layers at different compression loads and grafting densities. Notations are the same as in Figure 8.

the width of the overlap function decreases with increasing shear rate. This transformation of the overlap function results in a decrease of the effective interaction between two brush layers and the shear thinning regime seen in Figures 8 and 10.

A qualitatively different behavior between charged and neutral systems can also be seen in the dependence of the kinetic friction coefficient defined as the ratio between shear and compression stresses:

$$\mu(\dot{\gamma}) = \frac{\sigma_{yz}(\dot{\gamma})}{\sigma_{zz}} \quad (10)$$

Note that our simulations were done at constant compression stress; thus, the compression stress, σ_{zz} , is independent of the shear rate. The dependence of the friction coefficient, μ , on the shear rate is shown in Figure 12. The values of the friction coefficient for charged systems are about one order of magnitude smaller than corresponding values for neutral bottle-brush systems. This provides further support of the idea of the leading role of counterions in lubrication of charged bottle-brush layers. For all systems the friction coefficient increases with increasing brush grafting density. Note that the plots of μ vs $\dot{\gamma}$ provide a slightly different representation of the data shown in Figure 8.

The plateau regimes seen in Figure 8 correspond to the linear regime, $\mu \propto \dot{\gamma}$, while a sublinear increase in the friction coefficient, $\mu \propto \dot{\gamma}^\delta$ with $\delta < 1$, corresponds to shear thinning regimes seen in Figure 8.

4. CONCLUSIONS

We performed molecular dynamics simulations to study lubricating properties of charged and neutral bottle-brush layers. By varying the compression and shear stresses on the confined brush layers, we elucidated the effect of the brush grafting density and shear rate on deformation of the bottle-brush macromolecules, on the shear viscosity, and on the friction coefficient.

For charged bottle-brush systems we have shown that the deformation of the charged bottle-brush backbone is a universal function of the Weissenberg number, W (see eq 7). All data sets at different brush grafting densities and compression stresses have collapsed into one universal plot (see Figure 6). At large values of the Weissenberg numbers, $W \gg 1$, the size of the brush backbone increases with the shear rate as $R^2 \propto \dot{\gamma}^{0.32}$. However, at small Weissenberg numbers, $W \ll 1$, the deformation ratio, α , is on the order of unity and shear stresses are too weak to overcome backbone deformation induced by the electrostatic interactions between charged monomers. The value of the crossover shear rate, $\dot{\gamma}^*$, increases monotonically with the brush grafting density, ρ_g . Neutral systems also show an increase of the bottle-brush backbone deformation with increasing shear rate. However, only data sets corresponding to low compression stress can be fitted together to eq 7 with the same value of the exponent $\beta = 0.77$ within a finite interval of shear rates. In the case of high compression the exponent β depends on the brush grafting density (see Table 1). This can be explained by a stronger effect of the side chain deformation on the conformation of the brush backbone with increasing shear rate observed for neutral bottle-brush systems in comparison with that for charged systems (see Figure 9). The crossover shear rate, $\dot{\gamma}^*$, changes nonmonotonically with the brush grafting density. Also these values are smaller for all brush grafting densities and compression stresses in comparison with corresponding values for charged bottle-brushes. This is due to stronger deformation of the charged bottle-brush macromolecules in unperturbed brush layers.

The universality in the charged bottle-brush backbone deformation manifests itself in universal behavior of the shear viscosity with the Weissenberg number, W (see Figure 10a). The linear bottle-brush deformation regime with $\eta \approx \eta_0$ is followed by the nonlinear shear thinning regime with $\eta \propto W^{-0.53}$. This universal behavior of the charged bottle-brush systems is a result of formation of a lubricating layer of counterions separating two bottle-brush layers (see Figures 4 and Figure 3A–D). There is no such universality for neutral bottle-brush systems (see Figure 10b). The viscosity of the neutral bottle-brush systems has two plateau regimes and two shear thinning regimes. The second plateau becomes less pronounced with increasing brush grafting density and compression stress. The first plateau and shear thinning regime can be associated with the brush backbone deformation, while the second plateau and shear thinning regime are due to deformation of the side chains. At high shear rates bottle-brush backbones are aligned along the substrate with side chains pointing away from the grafting substrate such that the structure of the bottle-brush layer resembles that of the brush of linear chains (see Figure 3H,P). In this high shear rate regime the side

chains determine the strength of the interactions between brush layers and control lubrication.

Let us comment on the effect of the explicit solvent. In simulations with the explicit solvent, the hydrodynamic interactions between bottle-brush chains can lead to quantitatively different values of the exponents for backbone deformation and shear viscosity with the Weissenberg number, W , as well as result in a shift of the crossover value of the shear rate, $\dot{\gamma}^*$, and modification of its dependence on the system parameters.³³ However, we do not expect qualitative changes in system behavior. For charged bottle-brush systems we still expect a dominant role of counterions in the lubrication process. Furthermore, molecular dynamics simulations of polyelectrolyte solutions⁶¹ have shown that scaling exponents for dynamic properties of polyelectrolyte solutions obtained from simulations without explicit solvent are close to experimental scaling exponents. This was explained by the long-range nature of both hydrodynamic and electrostatic interactions. Thus, for charged systems even simulations without explicit solvent can correctly reproduce the system dynamics. The detailed study of the effect of the explicit solvent on lubrication will be addressed in future publications.

ACKNOWLEDGMENT

This work was supported by the National Science Foundation under Grant DMR-1004576.

REFERENCES

- (1) Granick, S.; Kumar, S. K.; Amis, E. J.; Antonietti, M.; Balazs, A. C.; Chakraborty, A. K.; Grest, G. S.; Hawker, C. J.; Janmey, P.; Kramer, E. J.; Nuzzo, R.; Russell, T. P.; Safinya, C. R. *J. Polym. Sci., Part B: Polym. Phys.* **2003**, *41*, 2755–2793.
- (2) Grest, G. S. *Curr. Opin. Colloid Interface Sci.* **1997**, *2*, 271–277.
- (3) Kato, K.; Uchida, E.; Kang, E. T.; Uyama, Y.; Ikada, Y. *Prog. Polym. Sci.* **2003**, *28*, 209–259.
- (4) Ruhe, J.; Ballauff, M.; Biesalski, M.; Dziezok, P.; Grohn, F.; Johannsmann, D.; Houbenov, N.; Hugenberg, N.; Konradi, R.; Minko, S.; Motornov, M.; Netz, R. R.; Schmidt, M.; Seidel, C.; Stamm, M.; Stephan, T.; Usov, D.; Zhang, H. N. *Adv. Polym. Sci.* **2004**, *165*, 79–150.
- (5) Ballauff, M.; Borisov, O. *Curr. Opin. Colloid Interface Sci.* **2006**, *11*, 316–323.
- (6) Krim, J. *Surf. Sci.* **2002**, *50*, 741–758.
- (7) Lee, S.; Spencer, N. D. *Science* **2008**, *319*, 575–576.
- (8) Klein, J.; Kumacheva, E.; Perahia, D.; Mahalu, D.; Warburg, S. *Faraday Discuss.* **1994**, *98*, 173–188.
- (9) Klein, J.; Kumacheva, E.; Mahalu, D.; Perahia, D.; Fetters, L. J. *Nature* **1994**, *370*, 634–636.
- (10) Raviv, U.; Giasson, S.; Kampf, N.; Gohy, J. F.; Jerome, R.; Klein, J. *Nature* **2003**, *425*, 163–165.
- (11) Tadmor, R.; Janik, J.; Klein, J.; Fetters, L. J. *Phys. Rev. Lett.* **2003**, *91*, 115503.
- (12) Kampf, N.; Gohy, J. F.; Jerome, R.; Klein, J. *J. Polym. Sci., Part B: Polym. Phys.* **2005**, *43*, 193–204.
- (13) Dean, D.; Han, L.; Ortiz, C.; Grodzinsky, A. J. *Macromolecules* **2005**, *38*, 4047–4049.
- (14) Dean, D.; Han, L.; Grodzinsky, A. J.; Ortiz, C. *J. Biomech.* **2006**, *39*, 2555–2565.
- (15) Claesson, P. M.; Poptoshev, E.; Blomberg, E.; Dedinaite, A. *Adv. Colloid Interface Sci.* **2005**, *114*, 173–187.
- (16) Muller, M. T.; Yan, X. P.; Lee, S. W.; Perry, S. S.; Spencer, N. D. *Macromolecules* **2005**, *38*, 5706–5713.
- (17) Raviv, U.; Giasson, S.; Kampf, N.; Gohy, J. F.; Jerome, R.; Klein, J. *Langmuir* **2008**, *24*, 8678–8687.
- (18) Liberelle, B.; Giasson, S. *Langmuir* **2008**, *24*, 1550–1559.

- (19) Zappone, B.; Ruths, M.; Greene, G. W.; Jay, G. D.; Israelachvili, J. N. *Biophys. J.* **2007**, *92*, 1693–1708.
- (20) Pettersson, T.; Naderi, A.; Makuska, R.; Claesson, P. M. *Langmuir* **2008**, *24*, 3336–3347.
- (21) Dunlop, I. E.; Briscoe, W. H.; Titmuss, S.; Jacobs, R. M. J.; Osborne, V. L.; Edmondson, S.; Huck, W. T. S.; Klein, J. *J. Phys. Chem. B* **2009**, *113*, 3947–3956.
- (22) Chen, M.; Briscoe, W. H.; Armes, S. P.; Klein, J. *Science* **2009**, *323*, 1698–1701.
- (23) Goujon, F.; Malfreyt, P.; Tildesley, D. J. *Soft Matter* **2010**, *6*, 3472–3481.
- (24) Klein, J. *Proc. Inst. Mech. Eng., Part J* **2006**, *220* (J8), 691–710.
- (25) Han, L.; Dean, D.; Ortiz, C.; Grodzinsky, A. J. *Biophys. J.* **2007**, *92*, 1384–1398.
- (26) Han, L.; Dean, D.; Daher, L. A.; Grodzinsky, A. J.; Ortiz, C. *Biophys. J.* **2008**, *95*, 4862–4870.
- (27) Chan, S. M. T.; Neu, C. P.; DuRaine, G.; Komvopoulos, K.; Reddi, A. H. *Osteoarthritis Cartilage* **2010**, *18*, 956–963.
- (28) Coles, J. M.; Chang, D. P.; Zauscher, S. *Curr. Opin. Colloid Interface Sci.* **2010**, *15*, 406–416.
- (29) Binder, K. *Eur. Phys. J. E* **2002**, *9*, 293–298.
- (30) Currie, E. P. K.; Norde, W.; Stuart, M. A. C. *Adv. Colloid Interface Sci.* **2003**, *100*, 205–265.
- (31) Dean, D.; Seog, J.; Ortiz, C.; Grodzinsky, A. J. *Langmuir* **2003**, *19*, 5526–5539.
- (32) Sokoloff, J. B. *Macromolecules* **2007**, *40*, 4053–4058.
- (33) Galuschko, A.; Spirin, L.; Kreer, T.; Johner, A.; Pastorino, C.; Wittmer, J.; Baschnagel, J. *Langmuir* **2010**, *26*, 6418–6429.
- (34) Grest, G. S. *Phys. Rev. Lett.* **1996**, *76*, 4979–4982.
- (35) Doyle, P. S.; Shaqfeh, E. S. G.; Gast, A. P. *Macromolecules* **1998**, *31*, 5474–5486.
- (36) Saphiannikova, M. G.; Pryamitsyn, V. A.; Cosgrove, T. *Macromolecules* **1998**, *31*, 6662–6668.
- (37) Kreer, T.; Muser, M. H.; Binder, K.; Klein, J. *Langmuir* **2001**, *17*, 7804–7813.
- (38) Kreer, T.; Binder, K.; Muser, M. H. *Langmuir* **2003**, *19*, 7551–7559.
- (39) Schorr, P. A.; Kwan, T. C. B.; Kilbey, S. M.; Shaqfeh, E. S. G.; Tirrell, M. *Macromolecules* **2003**, *36*, 389–398.
- (40) Kreer, T.; Muser, M. H. *Wear* **2003**, *254*, 827–831.
- (41) Dimitrov, D. I.; Milchev, A.; Binder, K. *J. Chem. Phys.* **2007**, *127*, 084905.
- (42) Neelov, I. M.; Borisov, O. V.; Binder, K. *Macromol. Theory Simul.* **1998**, *7*, 141–156.
- (43) Neelov, I. M.; Borisov, O. V.; Binder, K. *J. Chem. Phys.* **1998**, *108*, 6973–6988.
- (44) Yin, F.; Bedrov, D.; Smith, G. D. *Eur. Polym. J.* **2008**, *44*, 3670–3675.
- (45) Sirchabesan, M.; Giasson, S. *Langmuir* **2007**, *23*, 9713–9721.
- (46) Cao, Q. Q.; Zuo, C. C.; Li, L. J.; He, H. W. *Modell. Simul. Mater. Sci. Eng.* **2010**, *18*, 075001.
- (47) Zhulina, E. B.; Vilgis, T. A. *Macromolecules* **1995**, *28*, 1008–1015.
- (48) Carrillo, J. M. Y.; Dobrynin, A. V. *Langmuir* **2010**, *26*, 18374–18381.
- (49) Cao, Q. Q.; Zuo, C. C.; Ma, Y. H.; Li, L. J.; Chen, S. Y.; Hu, Z. Y. *J. Polym. Sci., Part B: Polym. Phys.* **2011**, *49*, 882–889.
- (50) Russano, D.; Carrillo, J. M. Y.; Dobrynin, A. V. *Langmuir* **2011**, *44*, 11044–11051.
- (51) De Vos, W. M.; Leermakers, F. A. M.; Lindhoud, S.; Prescott, S. W. *Macromolecules* **2011**, *44*, 2334–2342.
- (52) Rubinstein, M.; Colby, R. H. *Polymer Physics*; Oxford University Press: New York, 2003.
- (53) Frenkel, D.; Smit, B. *Understanding Molecular Simulations*; Academic Press: New York, 2002.
- (54) Grest, G. S.; Murat, M. *Macromolecules* **1993**, *26*, 3108–3117.
- (55) Kremer, K.; Grest, G. S. *J. Chem. Phys.* **1990**, *92*, 5057–5086.
- (56) Hockney, R. W.; Eastwood, J. W. *Computer Simulations Using Particles*; Hilger-IOP: Bristol, 1988.
- (57) Plimpton, S. J. *Comput. Phys.* **1995**, *117*, 1–19. See also <http://lammmps.sandia.gov>.
- (58) Crozier, P. S.; Rowley, R. L.; Henderson, J. W. *J. Chem. Phys.* **2001**, *114*, 7513.
- (59) Thompson, P. A.; Robbins, M. O. *Phys. Rev. A* **1990**, *41*, 6830–6837.
- (60) Bird, R. B.; Armstrong, R. C.; Hassager, O. *Dynamics of Polymeric Liquids*; John Wiley & Sons: New York, 1987; Vol. 1.
- (61) Liao, Q.; Carrillo, J. M. Y.; Dobrynin, A. V.; Rubinstein, M. *Macromolecules* **2007**, *40*, 7671–7679.